ADVANCED OPTICAL MATERIALS
www.advopticalmat.de

Influence of Shell Thickness on the Photophysical Properties of Core—Shell Perovskite Nanocrystals

*Xuanyu Zhang, Chengxi Zhang, Baian Chen, Junzi Li, Zhaojin Wang, Kai Wang, Tingchao He, Xuyong Yang, and Rui Chen**

Core–shell perovskite nanocrystals (NCs) have emerged as a promising class of materials for optoelectronic applications due to their unique properties and stability. Although much research has been conducted on the shell growth mechanism and properties of the core–shell NCs, little is known about the role of shell thickness in determining their optical properties. Herein, a heteroepitaxial method is employed to prepare a series of core–shell $FAPbBr_3/CsPbBr_3$ NCs with different shell thicknesses. Through temperature-dependent photoluminescence measurement, it is found that the electronic structure of core–shell $FAPbBr_3/CsPbBr_3$ NCs evolves from quasi-type-II to type-I with the increase in shell thickness. This abnormal transition can be attributed to the thickened gradient alloy layer $FA_{1-x}Cs_xPbBr_3$, which effectively relieves the lattice mismatch and releases strain in the NCs, resulting in variations in the bandgap between the core and the shell. Furthermore, the biexciton Auger lifetimes in these samples exhibit a non-monotonic dependence on shell thickness, indicating the electronic structure transition. These results provide valuable insights into the relationship between shell thickness, electronic structure, and optical properties in core–shell perovskite NCs, which may offer guidance for the design of high-performance optoelectronic devices.

1. Introduction

Recently, lead halide perovskite nanocrystals (NCs) have emerged as the main competitors to replace conventional semiconductor NCs due to their intriguing properties such as high photoluminescence quantum yield (PLQY), excellent color purity, compositional and bandgap tunability,[1–3] which has promoted their applications in light-emitting diodes, solar cells, photodetectors, lasers, bioimaging, and so on.[4–8] However, the instability problem in the ambient atmosphere will not only lead to the decomposition and transformation of perovskite NCs, but also result in luminescence quenching and poor electron mobility, which seriously hinders their practical applications and commercial scalability.[9] In the past few years, tremendous research efforts have been made to overcome these limitations.[10–13] Among them, the core–shell structure is one of the most classical strategies, which not only effectively suppresses the interaction between the NCs, but also passivates the surface defect states.[14] More importantly, the core–shell structure endows perovskite NCs with new properties, improves their performance, and expands their application in optoelectronic devices. To date, the developments of core–shell perovskite NCs have been very extensive.[15–17] The choice of shell includes metals, traditional semiconductors, insulators, metal–organic frameworks, or polymer materials. However, due to the ultrafast growth dynamics of perovskite NCs, softer lattice, and coordination of ionic bonds, it is difficult to control the secondary epitaxial growth of these materials on perovskite NCs surface, which greatly limits the application of core–shell perovskite NCs. In addition, the large lattice mismatch between other materials and perovskites inevitably leads to the loss of device performance. Therefore, perovskite-perovskite core–shell NCs may be the optimal solution.

In 2016, N. Mathews et al. first demonstrated the development of highly stable and color-tunable perovskite-perovskite core–shell $MAPbBr_3/(OA)_2PbBr_4$ NCs based on ligand-assisted reprecipitation strategy.[18] The core–shell NCs exhibited tunable emission from the blue to a green spectral region (438–521 nm), high PLQY, and excellent stability. Under ambient conditions, the initial observed PLQY of 92% for the core–shell NCs showed only a slight decrease with time, reaching a value of 85% after one

X. Zhang, B. Chen, Z. Wang, K. Wang, R. Chen
Department of Electrical and Electronic Engineering
Southern University of Science and Technology
Shenzhen 518055, P. R. China
E-mail: chenr@sustech.edu.cn
C. Zhang, X. Yang
Key Laboratory of Advanced Display and System Applications of Ministry of Education Shanghai University
Shanghai 200072, P. R. China
J. Li, T. He
College of Physics and Optoelectronic Engineering
Shenzhen University
Shenzhen 518060, P. R. China
C. Zhang
Department of Optoelectronic Information Science and Engineering
School of Science
Jiangsu University of Science and Technology
Zhenjiang, Jiangsu 212100, P. R. China

The ORCID identification number(s) for the author(s) of this article can be found under https://doi.org/10.1002/adom.202301782

DOI: 10.1002/adom.202301782

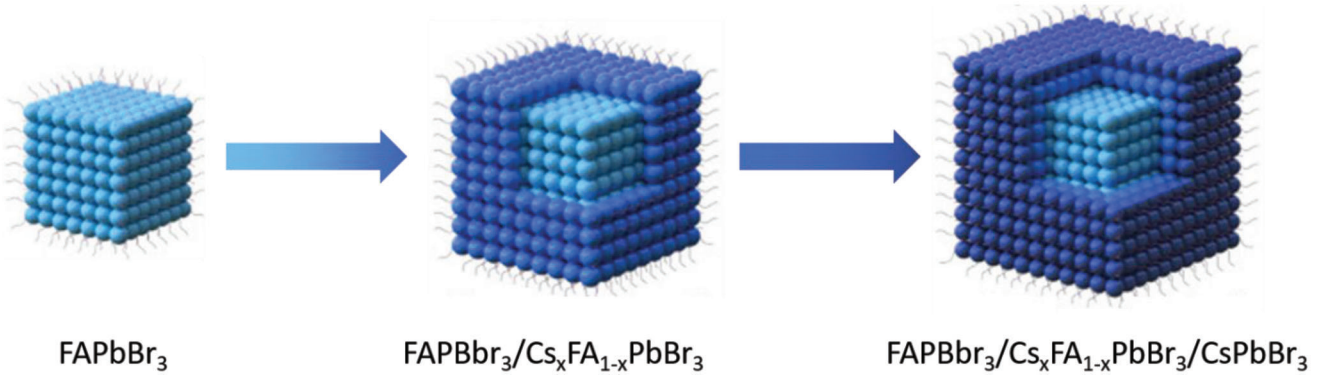

Figure 1. The schematic illustration of the synthesis process of core/shell $FAPbBr_3/CsPbBr_3$ NCs.

month and 60% after two months. While the initial 84% PLQY observed for $MAPbBr_3$ NCs showed a significant decrease over time, reaching a value of 45% after one month and completely quenched after two months. Moreover, this type of core–shell NCs exhibited a huge five-photon action cross-section which is at least 9 orders larger than the state-of-the-art specially designed organic molecules, enabling new approaches for next-generation multiphoton imaging applications.[19] Subsequently, the core–shell $CsPbBr_3/Cs_4PbBr_6$ NCs were prepared by a seeded growth method.[20] The Cs_4PbX_6 shell with a wider bandgap was selected to achieve effective confinement of excitons, which results in a high PLQY. On this basis, the polaron-mediated slow carrier cooling in $CsPbBr_3/Cs_4PbBr_6$ NCs was investigated, which enriches their potential in the photovoltaic field.[21] In addition, we have fabricated the core–shell $FAPbBr_3/CsPbBr_3$ NCs via a heteroepitaxial method.[22] These NCs can be stored under ambient conditions for up to 70 days, and after 50 h of ultraviolet (UV) irradiation, they still exhibited excellent stability and retained more than 80% of the initial PLQY. Meanwhile, the maximum current efficiency observed in the core–shell NCs LED was 19.75 cd A^{-1} and the external quantum efficiency was 8.1%. Compared with the core-only devices, these two parameters are about four and eight times higher, respectively.

Obviously, benefited from the shell growth, all of the above core–shell perovskite NCs exhibited improved stability. Of particular importance, the shell also possesses a decisive influence on the optoelectronic properties of the entire core–shell structure. It is generally accepted that the shell thickness affects the degree of defect state passivation, the structure of the energy band, the dynamics of carriers, and so on.[23,24] Unfortunately, to date, the reports on the influence of shell thickness on the photophysical properties in core–shell perovskite NCs are still insufficient. To address this issue, in this work, the thickness-controlled $FAPbBr_3/CsPbBr_3$ NCs were prepared according to the previously reported method.[22] The prepared NCs were characterized by steady-state absorption, photoluminescence (PL), X-ray diffraction (XRD), and high-resolution transmission electron microscope (HRTEM) techniques. The electronic structures in core–shell $FAPbBr_3/CsPbBr_3$ NCs with different shell thicknesses were studied by temperature-dependent PL spectroscopy. Interestingly, in contrast to conventional semiconductor NCs, the transition from quasi-type-II to type-I occurred with the increase of thickness in the core–shell perovskite NCs. This transition was attributed to the thickened gradient alloy layer $FA_{1-x}Cs_xPbBr_3$, which renormalized the valence bands of both the core and the shell through strain release. Furthermore, femtosecond pump-probe transient absorption spectroscopy was employed to investigate their carrier dynamics. The results showed that the biexciton Auger lifetimes in core–shell NCs initially increased significantly, and then decreased with increasing shell thickness, providing further evidence for the electronic structure transformation.

2. Results and Discussion

Figure 1 shows the synthesis of core/shell $FAPbBr_3/CsPbBr_3$ NCs. In the process of forming the core–shell structure, a gradient alloy layer $FA_{1-x}Cs_xPbBr_3$ is first grown on the core $FAPbBr_3$ by ion exchange. And then, based on the alloy layer, the $CsPbBr_3$ shell is grown. The molar ratio, *X*, of Cs to FA with $X = 0.5$, 1.0, and 2.0, to produce the core–shell structures with different shell thicknesses. **Figure 2**a–d presents the detailed morphological investigation of the core–shell $FAPbBr_3/CsPbBr_3$ NCs with different shell thicknesses (X = 0.0, 0.5, 1.0, and 2.0). All the NCs exhibit a cubic shape with an average size of 8.10, 9.60, 11.30, and 15.00 nm, respectively. The insets show the HRTEM images showing the corresponding crystal spacing of ≈3.00, 3.77, 4.30, and 4.81 Å, respectively. The increase of the average size and crystal spacing reveals the formation of a shell with thicknesses of 0.00, 0.75, 1.60, and 3.45 nm for $X = 0.0$, 0.5, 1.0, and 2.0, respectively. It is noteworthy that some small black particles can be observed in Figure 2d, which may be caused by the reduction of Pb^{2+} ions to Pb^0 atoms,[25] followed by their diffusion and aggregation. This suggests a lack of bromine atoms in thicker shells, leading to a high density of defect states. Meanwhile, the fast Fourier transform patterns in Figure S1 (Supporting Information) show that with the increase in *X*, the crystal quality of the core–shell NCs gradually improves, and it reaches the optimal situation at $X = 1.0$. Subsequent continuous increases in the amount of Cs will result in a significant decrease in crystal quality. Figure S2 (Supporting Information) shows the TEM energy dispersive X-ray elemental mapping of the four samples to observe the distribution of different atoms. XRD characterization was performed to further investigate the structural characteristics of the NCs with different $CsPbBr_3$ shell thicknesses. As shown in Figure 2e, the $FAPbBr_3$ NCs have the primary

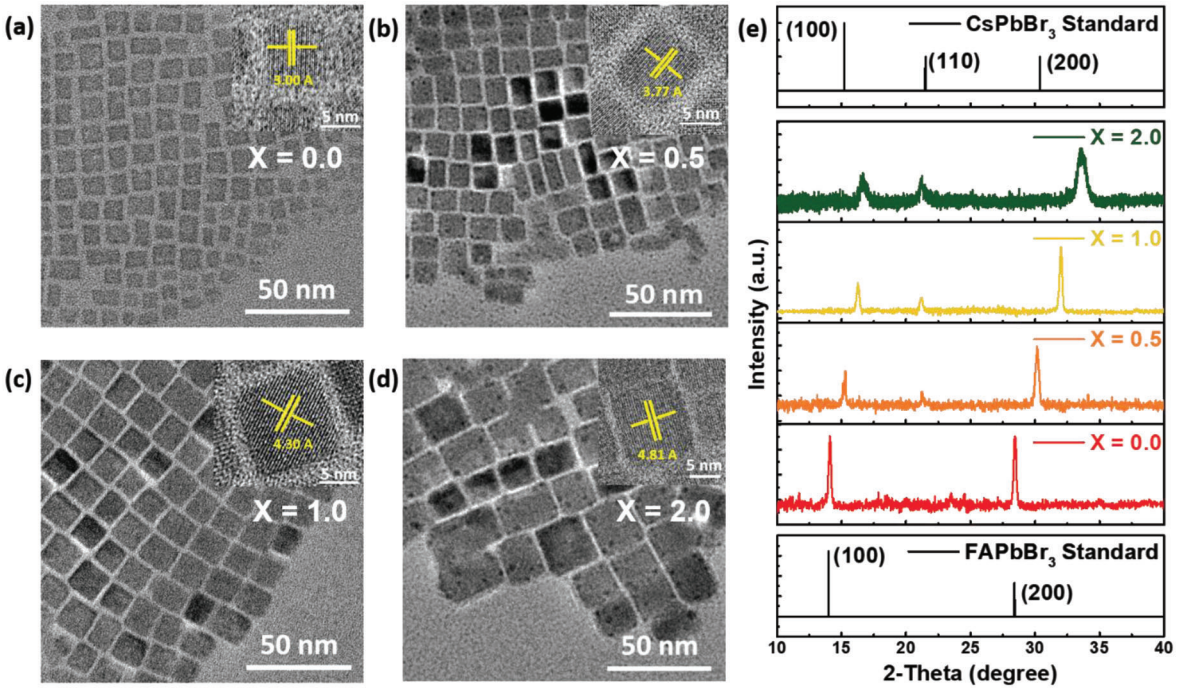

Figure 2. a–d) TEM images and e) XRD patterns of the core–shell $FAPbBr_3/CsPbBr_3$ NCs with different thickness control (the values of X are the different molar ratios of Cs/FA). The insets in (a–d) are the corresponding HRTEM images of these four samples.

diffraction peaks at 14.8° and 29.8°, which can be assigned to the (100) and (200) planes of cubic perovskite.[22] After the growth of the all-inorganic $CsPbBr_3$ shell, the diffraction peaks of the $FAPbBr_3/CsPbBr_3$ NCs shift to larger angles with increasing molar ratio of Cs: FA from 0.5 to 2.0. This observation is consistent with Vegard's law,[26,27] which confirms the absence of alloyed perovskite NCs. Accordingly, it is suggested that a transition layer of the $FA_{1-x}Cs_xPbBr_3$ alloy is formed between the organic-inorganic core and all-inorganic shell. The low signal-to-noise ratio observed in the XRD spectra for the NCs with $X = 2.0$ can be attributed to the abundance of defect states in the NCs, which is consistent with the observation from the TEM images. In addition, excessive shell thickness leads to more defect states, which further reduces the signal intensity.

The UV–vis absorption and PL spectra of the NCs with and without shell measured at room temperature are displayed in **Figure 3**a. The PL spectrum of $FAPbBr_3$ NCs is peaking at 535.6 nm with a full width at half maximum (FWHM) of 21.0 nm, which is slightly redshifted from the absorption band. After shell growth, the optical properties of the NCs change, with a blueshift observed with the increase in shell thickness. For $X = 2.0$, the PL emission is centered at 519.2 nm, and the FWHM is reduced by 4.3 nm. The blueshift in the PL emission of core–shell NCs can be mainly attributed to the formation of an alloy layer of

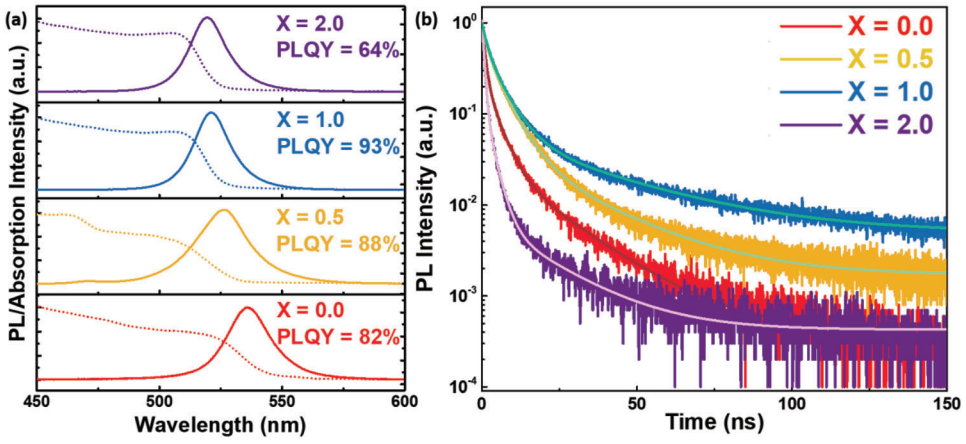

Figure 3. a) UV–vis absorbance and PL spectra and b) time-resolved PL decay curves of the core–shell $FAPbBr_3/CsPbBr_3$ NCs with different shell thicknesses.

Table 1. The PLQY and corresponding radiative and non-radiative rate constants of the core–shell NCs with different shell thicknesses.

X	PLQY [%]	Average Lifetime [ns]	Radiative Rate Constant [ns^{-1}]	Non-radiative Rate Constant [ns^{-1}]
0.0	82	13.9	0.059	0.013
0.5	88	19.5	0.045	0.006
1.0	93	26.2	0.043	0.003
2.0	64	7.4	0.086	0.049

FA_{1-x} Cs_xPbBr_3 at the core–shell interface of NCs, which results in a reduced effective size of the $FAPbBr_3$ core. In principle, this will lead to a continuous and significant blueshift of the emission. However, with the increase of shell thickness, this blueshift becomes less pronounced, which may be due to the strain relaxation. Based on the density functional theory (DFT) calculation as shown in Figure S11 (Supporting Information), the increased thickness of the alloy layer promotes strain relaxation, which slows down the bandgap increase of the core $FAPbBr_3$ NCs. Meanwhile, the long-range, infinite lattice periodicity of a core NC is disturbed during the shell coating process, and the differences in dielectric constant and absorption coefficient between the core and shell also affect the physical properties of the perovskite NCs. This gradual change in optical properties is consistent with the results obtained from XRD and supports the hypothesis of the formation of an alloyed transition layer. Therefore, it can be concluded that the all-inorganic shell of $CsPbBr_3$ is formed over the alloyed transition layer as the Cs content increases. In addition, the more pronounced absorption signals in the core–shell NCs with $X = 1.0$ and 2.0 are consistent with increasing strength of exciton confinement in $FAPbBr_3$ for NCs capped with a thicker $CsPbBr_3$ shell. For the core–shell NCs with $X = 0.5$, an absorption peak at 460 nm can be observed, which is related to the residual $CsPbBr_3$ nanoplatelets, as shown in Figure 2b. It is needed to mention that $CsPbBr_3$ nanoplatelets have been preferentially formed in the presence of a small amount of Cs source, and it is quite difficult to completely remove them even after purification. Furthermore, the PLQY is increased from 82% for $X = 0.0$ to a maximum value of 93% for $X = 1.0$ by overgrowing the NCs with an inorganic shell. However, for the core–shell NCs with $X = 2.0$, the value of PLQY is only 64%, presumably due to the high density of defect states. Meanwhile, time-resolved PL (TRPL) experiments were conducted to understand the dynamics of carrier recombination, and the data is shown in Figure 3b. The decay times can be well-fitted with a triexponential function[28]

$$A(t) = A_1 \exp\left(-\frac{t}{\tau_1}\right) + A_2 \exp\left(-\frac{t}{\tau_2}\right) + A_3 \exp\left(-\frac{t}{\tau_3}\right) \quad (1)$$

where A_1, A_2, and A_3 are weight, t is time, and τ_1, τ_2, and τ_3 represent the decay lifetimes corresponding to the intrinsic defects, surface states, and exciton recombination, respectively (Table S1, Supporting Information). The average PL lifetime (τ_{ave}) can be calculated as

$$\tau_{ave} = \frac{A_1\tau_1^2 + A_2\tau_2^2 + A_3\tau_3^2}{A_1\tau_1 + A_2\tau_2 + A_3\tau_3} \quad (2)$$

As X increases, corresponding to an increase in shell thickness, the derived τ_{ave} of $FAPbBr_3/CsPbBr_3$ NCs exhibits the same trend as that of PLQYs. The value increases from 13.9 ns for $FAPbBr_3$ NCs to 26.6 ns for $FAPbBr_3/CsPbBr_3$ NCs with $X = 1.0$. In order to understand the exciton recombination, the radiative and non-radiative decay rates were calculated using PLQY and the average lifetime, as shown in **Table 1**. The radiative rate decreased slightly from 0.059 to 0.035 ns^{-1}, and the non-radiative recombination, which must be controlled for optical properties, significantly decreased from 0.013 to 0.003 ns^{-1}. Therefore, the improvement in PL performance can be attributed to the greatly reduced non-radiative attenuation in the core–shell structure. On the other hand, when an excessively thick shell is formed, the non-radiative rate increases to 0.049 ns^{-1}, which confirms the higher defect state densities. These observations confirm that moderate shell growth provides more efficient passivation of surface defects on $FAPbBr_3$ NCs, leading to a reduction in the number of nonradiative recombination centers. However, overgrowth of the shell could introduce more defect states.

To better understand the influence of shell thickness on the carrier dynamics in core–shell NCs, temperature-dependent PL experiments were performed (Figure S3, Supporting Information). It can be clearly seen in **Figure 4**a that the PL spectra of core–shell NCs with $X = 0.5$ and 1.0 at 50 K are quite different from those of $X = 0.0$ and 2.0. Specifically, two PL emissions are observed at low temperatures for $X = 0.5$ and 1.0, while only one PL emission is observed for $X = 0.0$ and 2.0 with the temperature increases from 50 to 295 K. In the former case, the PL emission at low temperature can be divided into Peak 1 located at high energy, and Peak 2 at low energy (Figure S4, Supporting Information). It is worth noting that the appearance of two separate emissions of the NCs with $X = 0.5$ and 1.0 at low temperatures is not due to the change of crystal phase. For $FAPbBr_3$ NCs ($X = 0.0$), there is a significant redshift of the emission with phase transition from orthorhombic to tetragonal due to the change of bandgap, as shown in Figure S4a (Supporting Information). However, for the core–shell NCs with $X = 0.5$ and 1.0, both emissions continuously blueshift with the increase in temperature. Moreover, the emitted photon energy is inconsistent with the bandgap corresponding to the tetragonal phase. With the increase in temperature, Peak 2 gradually decreases and finally disappears, which is consistent with our previous report,[29] indicating that the core–shell NCs with $X = 0.5$ and 1.0 possess a quasi-type-II electronic structure. It is worth noting that the core–shell NCs with $X = 0.5$ and 1.0 are not exactly the same. At 200 K, Peak 2 persists in $X = 0.5$, while for $X = 1.0$, Peak 2 has completely disappeared, and Peak 1 dominates the emission. The FWHMs of these four samples are extracted and plotted in Figure 4b, and it is clear that as the shell thickness increases, the temperature at which Peak 2 disappears

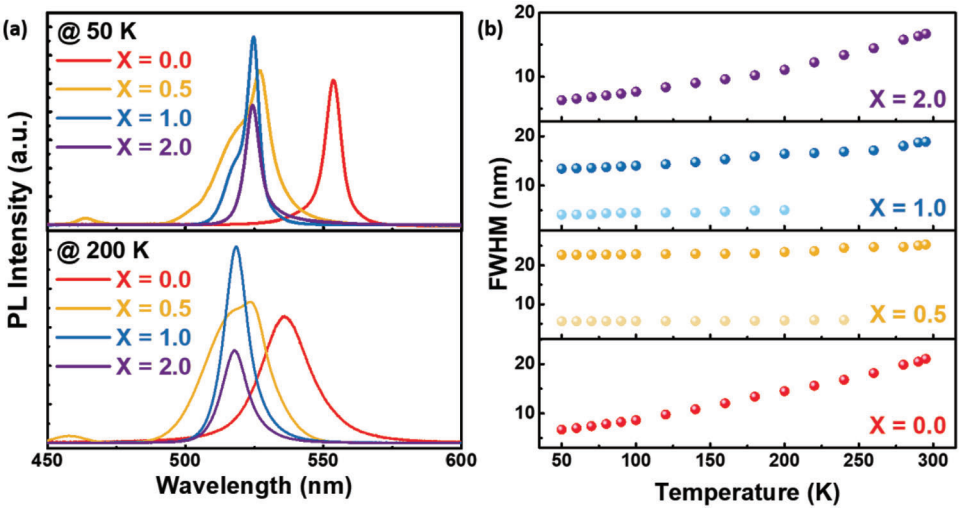

Figure 4. a) The PL spectra of the core–shell $FAPbBr_3/CsPbBr_3$ NCs with different shell thicknesses at 50 and 200 K. b) Temperature dependence of the FWHM for these four samples.

in core–shell NCs gradually decreases. For the core–shell NCs with $X = 2.0$, Peak 2 does not appear, so it can be assumed that the temperature at which it disappeared is 0 K. More importantly, compared with core–shell NCs with $X = 0.0$, the core–shell NCs with $X = 2.0$ exhibit narrower FWHM at each temperature, which is the representative feature of type-I band alignment. Based on the above observation, the hypothesis was proposed that the shell thickness renormalizes the electronic structure of the core–shell NCs, from quasi-type-II to type-I.

It is well known that the biexciton recombination lifetime (τ_{XX}) of the core–shell structure with quasi-type-II band alignment increases with the total volume of the NCs. However, for the type-I band alignment, τ_{XX} is independent of the NC volume. This provides an effective method to determine changes in the electronic structure of the core–shell NCs with different shell thicknesses.[24] To determine the τ_{XX} of the core–shell NCs studied here, pump-fluence-dependent transient absorption spectroscopy was performed (Figures S5–S8, Supporting Information). In addition, the time-resolved transient absorption spectra were displayed in Figure S9 (Supporting Information). **Figure 5**a–d displays the pump-fluence-dependent ground state blenching (GSB) decay processes of the core–shell NCs with $X = 0.0$, 0.5, 1.0, and 2.0. It can be seen that at low pump fluence, single exciton states dominate the photoexcited core–shell NCs, resulting in generally long-lived signals. With the increase of pump fluence, the amplitude of a new fast decay component

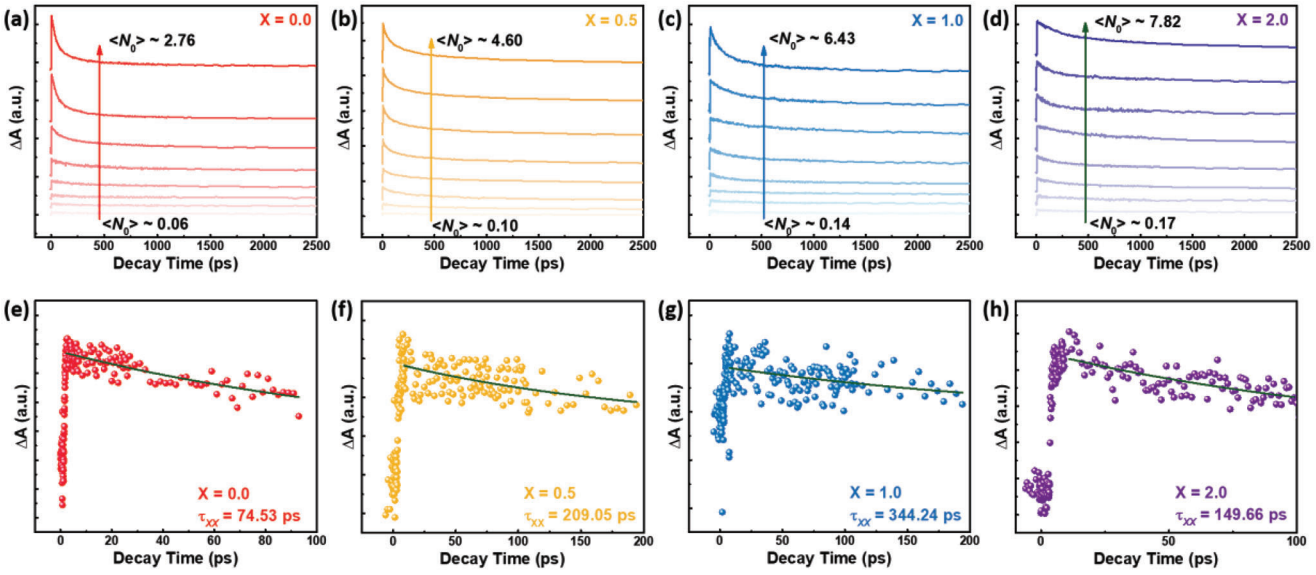

Figure 5. a–d) GSB decay curves for the core–shell $FAPbBr_3/CsPbBr_3$ NCs under different excitation intensities. e–h) The corresponding biexciton Auger recombination lifetimes.

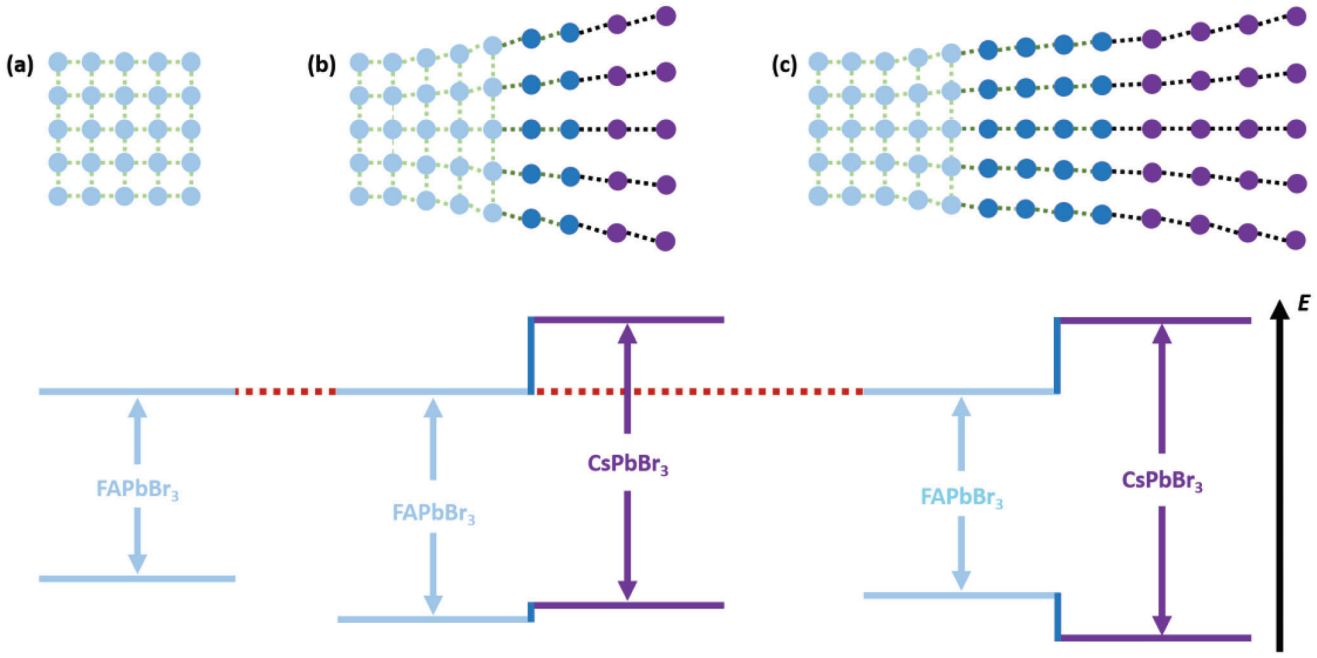

Figure 6. a-c) Schematic illustration of the strain and electronic structure in the core–shell $FAPbBr_3/CsPbBr_3$ NCs with different shell thicknesses.

becomes progressively larger, which is consistent with Auger recombination of multiple exciton states. Following the procedures discussed in previous literature,[30,31] the GSB decay curves were normalized to a long decay time (3 ns), and subtracted from the GSB curve under the lowest fluence pumping. The extracted kinetics are suitable for single-exponential decay fitting in Figure 5e–h, yielding τ_{XX} values of 74.53, 209.05, 344.24, and 149.66 ps for the core–shell NCs with $X = 0.0$, 0.5, 1.0, and 2.0, respectively.

For the core–shell NCs with $X = 0.5$ and 1.0, the τ_{XX} exhibits a significant increase in shell thickness, consistent with the predicted delocalization of the hole wave function in quasi-type-II core–shell NCs. This phenomenon reduces the overlap of the electron and hole wave functions, thereby decreasing the Coulombic Auger recombination rate, especially for thicker shells. In contrast, only a small increase of τ_{XX} has been observed for core–shell NCs with $X = 2.0$ compared to $X = 0.0$, consistent with type-I electronic structure. The relatively large band offset in this system confines the electron wave function within the core, resulting in negligible spatial separation between the electron and hole. Therefore, the modest increase in τ_{XX} can be attributed to the increased volume of the core–shell NCs.

It is necessary to provide a detailed explanation for the observed changes in electronic structure with increasing shell thickness because this phenomenon is contrary to most existing research findings.[23,32] For core–shell NCs, the change in electronic structure can be attributed to interfacial strain due to the lattice constant difference between the core and shell materials. Specifically, the strain (s) in a thin epitaxial shell layer with a lattice constant of a_2 grown on a core with a lattice constant of a_1 can be quantified by the misfit parameter (f), which is given by[33]

$$s = f - \frac{a_2 - a_1}{a_1} \tag{3}$$

However, in most finite-size heteroepitaxial core–shell structures, the core material also experiences the mismatch strain due to the interactive stress at the core–shell interface. Assuming that a shell with a thickness of l_2 is deposited on a core of diameter l_1, the strain perpendicular to the growth direction in the core and shell can be estimated by[34]

$$s_{core} = \frac{a_1 - a_{\|}}{a_1} \tag{4}$$

$$s_{shell} = \frac{a_2 - a_{\|}}{a_2} \tag{5}$$

$$a_{\|} = \frac{a_2 G_2 l_2 + a_1 G_1 l_1}{G_2 l_2 + G_1 l_1} \tag{6}$$

where $a_{\|}$ is the common lattice constant shared by the core and shell, and G_1 and G_2 are the shear moduli of the core and shell components. Obviously, the positive or negative value of s in Equations (4) and (5) indicates the compressive or tensile strain, respectively. Accordingly, the total strain energy (E) can be estimated by[33]

$$E = E_{core} + E_{shell} = 2Al_1 G_1 s_{core}^2 \frac{1+\nu_1}{1-\nu_1} + 2Al_2 G_2 s_{shell}^2 \frac{1+\nu_2}{1-\nu_2} \tag{7}$$

where A is the interfacial area, and ν_1 and ν_2 are the Poisson's ratios of the core and shell, respectively. It is clear from Equation (7) that the strain accumulation occurs rapidly with the increase of shell thickness. In real NCs, the magnitude of the strain typically varies in space. The strain is locally defined in each infinitesimal

Table 2. Strain-dependent bandgap of $CsPbBr_3$/$FAPbBr_3$ materials.

Strain	Calculated Bandgap Values [eV]	
	$CsPbBr_3$ (Compressive)	$FAPbBr_3$ (Tensile)
0%	2.376	2.229
1%	2.338	2.264
2%	2.289	2.295
3%	2.229	2.428
4%	2.158	2.579
5%	2.075	2.622

volume by a strain tensor, which is the gradient of the displacement vector with respect to position, as described below[35,36]

$$s_{ij} = \frac{1}{2}\left(\frac{\partial u_i}{\partial x_j} + \frac{\partial u_j}{\partial x_i}\right)(i,j = 1,2,3) \quad (8)$$

where u_1, u_2, and u_3 are the components of the displacement vector in the x, y, and z directions, which are designated as x_1, x_2, and x_3, respectively. Note that each component of $\boldsymbol{u}$ is a function of x, y, and z. Therefore, the introduction of an alloy layer between the core and shell triggers strain relaxation processes that release excess strain energy, thereby minimizing the overall Gibbs energy and contributing to structure stabilization. This strain release also mitigates the effect of strain on the energy band.[37] For the core–shell NCs studied in this work, the lattice constants of the core and shell are 3.00 and 5.84 Å,[38,39] respectively. The core and shell experience tensile and compressive strains, respectively. As shown in **Figure 6**b, the alloy layer $FA_{1-x}Cs_xPbBr_3$ spatially allows for a slow release of this strain. In addition, thicker alloy layers improve the gradient distribution of materials from the same components, leading to better strain release as schematically shown in Figure 6c. To support the strain modulation mechanism, DFT calculations were applied to investigate the strain-dependent bandgap variation of pure $FAPbBr_3$/$CsPbBr_3$ lattices (shell and core), respectively. Detail calculation settings are presented in Experimental Section and related information such as lattice configuration is provided in Supporting Information (Figures S10 and S11, Supporting Information). **Table 2** lists the calculated bandgap values of $FAPbBr_3$/$CsPbBr_3$ materials under different strains. The bandgap of $FAPbBr_3$ increases from 2.229 to 2.622 eV with increasing tensile strain, and that of $CsPbBr_3$ decreases from 2.376 to 2.075 eV with increasing compressive strain. It can be concluded that the $FAPbBr_3$ lattices have higher bandgap values under tensile strain, while the $CsPbBr_3$ lattices will shrink their bandgap when compressing. It is well-known that the valence band maximum (VBM) is more sensitive to strain.[40] Therefore, the bandgap renormalization in perovskite is equivalent to the VBM rearrangement. As shown in Figure 6, the strain release results in a decrease in the bandgap of the core and an increase in the bandgap of the shell. In other words, due to the upward and downward trend in VBM for the core and shell, respectively, the electronic structure shows a transformation from quasi-type-II to type-I with the increase of shell thickness.

The photostability of the NCs is of paramount importance for their application in optoelectronic devices. It is expected that the shell thickness will seriously affect the stability of the core–shell NCs. As shown in **Figure 7**, with continuous irradiation of ultraviolet laser (wavelength of 325 nm with power of 2.0 mW) for 12 h, the core–shell perovskite NCs show better stability in terms of the emission peak position and intensity. Specifically, the peak position of the core-only NCs ($X = 0.0$, $FAPbBr_3$) shifts from 535.5 to 546.5 nm (redshift of 11.0 nm), while for the core–shell NCs with $X = 0.5$, 1.0 and 2.0, the peak redshifts are 3.1, 1.9 and 5.4 nm, respectively. Moreover, with continuous irradiation, the PL intensity of the core-only NCs is attenuated up to 45%, while the attenuations of the core–shell NCs with $X = 0.5$, 1.0, and 2.0 are 39%, 19%, and 49%, respectively. It is noted that the core–shell NCs with $X = 2.0$ show poorer photostability than $X = 0.0$, which could be attributed to more defect states.

3. Conclusion

In summary, this study investigated the effect of shell thickness on core–shell perovskite NCs by temperature-dependent PL technique. The results showed a transformation of the electronic

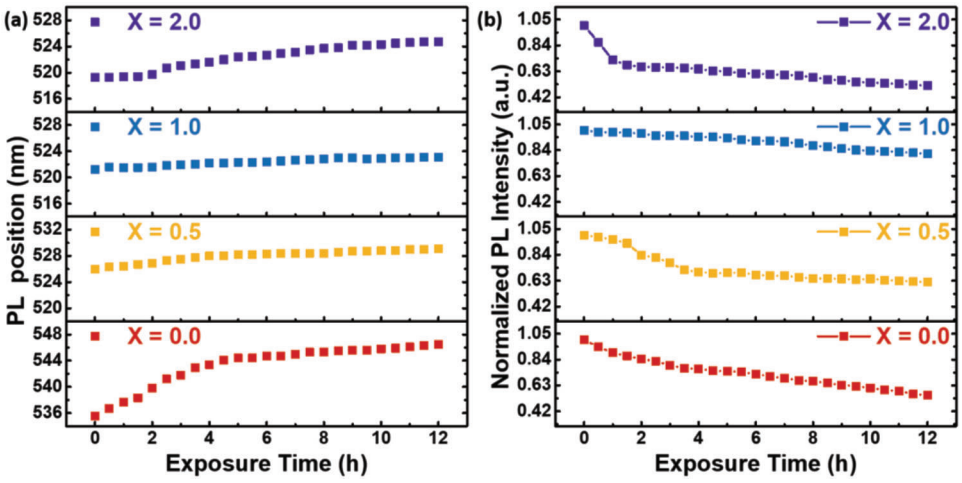

Figure 7. The photostability of the PL position (a) and intensity (b) of the core–shell NCs.

structure from quasi-type-II to type-I with the increase of the shell thickness. This phenomenon was attributed to the increased alloying of $FA_{1-x}Cs_xPbBr_3$, which formed a better gradient and released lattice strain, leading to the rearrangement of the energy levels in the core–shell NCs. In addition, femtosecond pump-probe transient absorption spectroscopy was utilized to study the biexciton Auger recombination in core–shell $FAPbBr_3/CsPbBr_3$ NCs with different shell thicknesses. It is found that the biexciton Auger lifetime initially increases and then decreases with increasing shell thickness, corroborating the observed change in electronic structure. These findings provide new insights into the design of NCs and their potential applications in high-efficiency optoelectronic devices.

4. Experimental Section

Synthesis of Perovskite Nanocrystals: All reagents were purchased and used without further purification: FA-acetate (Sigma-Aldrich), $Pb(CH_3COO)_2{\times}3H_2O$ (Sinopharm Chemical Reagent Co., Ltd., ≥99.5%), octadecene (ODE, Sigma–Aldrich, 90%), OA (Sigma–Aldrich, 90%), OAmBr (Xi'an Polymer Light Technology Crop), toluene (Sinopharm Chemical Reagent Co., Ltd., ≥99.5%), $PbBr_2$ (Sigma–Aldrich, 90%), Cs_2CO_3 (Sigma–Aldrich), OLA (Sigma–Aldrich, 90%). First, FA-acetate, $Pb(CH_3COO)_2{\cdot}3H_2O$, OA, and dried ODE were combined in 100 mL and dried for 30 min under vacuum at 50 °C. The mixture was heated to 130 °C under N_2 atmosphere and OAmBr in toluene was injected. After 10 s, the reaction mixture was cooled in ice-water bath. The green solution of $FAPbBr_3$ NCs was collected and stored at $T = 4$ °C. Next, $PbBr_2$ and Cs_2CO_3 were loaded into a 100 mL flask. The molar ratio, X, of Cs to FA with $X = 0.5$, 1.0, 2.0, was varied to produce core–shell structures with different shell thicknesses. Then, dried OA, dried ODE, dried OLA, and as synthesized $FAPbBr_3$ nanocrystals were added. The mixture was heated to 80 °C for 20 min under N_2 atmosphere, followed by cooling in ice bath. Finally, the resulting solution was centrifuged to remove undispersed residue and aggregated nanocrystals. The $FAPbBr_3/CsPbBr_3$ NCs dispersed in hexane were stored in the dark at $T = 4$ °C.

Structure Characterization: Samples for TEM measurement were prepared by dropping colloidal NCs solution with a relatively dilute concentration on carbon-coated 200 mesh copper grids. And the conventional TEM images were acquired by a Talos F200X microscope equipped with a thermionic gun under an acceleration voltage of 200 kV. The current of the 1 nm electron beam at this voltage is 1.5 nA, and the resolution is 0.12 nm. XRD patterns were recorded on a Bruker D8 Advance diffractometer with Cu Kα radiation ranging from 10° to 35° at a scanning rate of 4 min^{-1}.

Optical Characterization: UV–vis absorption spectra were recorded at room temperature on an UV–vis spectrophotometer (Lambda 950, PerkinElmer, Inc.). The PLQY was measured by Hamamatsu Quantaurus-QY with model No. C11347, which is an absolute quantum yield measurement device. After the samples are diluted to an absorption intensity of 0.3, they are placed in a quartz cuvette with an optical path of 1 cm. Then, the cuvette is placed in the integrating sphere. The continuous light emitted by the xenon lamp is divided by the monochromator, and introduced into the samples in the integrating sphere through the optical fiber. After the samples are excited, a fluorescence signal is generated, which is received by the back-end spectral detection system through the optical fiber. All PL spectra were recorded by a spectrometer (Andor SR-750) and detected using a charge-coupled device (CCD, model No. DU920P-BU). A continuous wave (CW) He-Cd gas laser with a laser line of 325 nm was used as the excitation source for temperature-dependent PL measurements. The samples were placed inside a closed-cycle helium cryostat (Cryo Industries of America) with quartz windows. The temperature during the PL measurement is well-controlled by a commercial temperature controller (Lakeshore 336) from 50 to 295 K. TRPL experiments were carried out at room temperature and the excitation source was a pulsed ultraviolet picosecond diode laser operating at 375 nm. The pulse width and repetition rate of the laser were 40 ps and 20 MHz, respectively. The signal was dispersed by a 320 mm monochromator (iHR320 from Horiba, Ltd.) combined with suitable filters and detected based on the time-correlated single photon counting (TCSPC) technique. Femtosecond pump-probe transient absorption measurement was conducted using a pump-probe spectrometer (Spectra-Physics, Inc.). A total of 800 nm pulses (100 fs, 1000 Hz) were first generated using a mode-locked Ti: sapphire laser. The beam was then split into two. One beam was used to generate a 350 nm excitation, and the second beam was passed through an optical delay line (with a time window of 3000 ps) and focused on a 2 mm thick sapphire to generate a white-light continuum (400–800 nm). The spectrum was dispersed on a cooled CCD.

DFT Calculations: The DFT calculations in this work were completed by the pseudopotential plane waves-based CASTEP module encapsulated in Materials Studio software.[41,42] The $FAPbBr_3/CsPbBr_3$ models were constructed with cubic phase and underwent precisive geometric optimization prior to the calculation of electronic properties. The self-consistent field iterations with a density-mixing electronic minimizer were applied to get suitable electronic distribution. Generalized gradient approximation (GGA) with the Perdew—Burke–Ernzerhof (PBE) functional was applied to deal with the exchange-correlation terms and Broyden—Fletcher–Goldfarb–Shannon (BFGS) algorithm was used to proceed with the structure relaxation.[43,44] Norm conserving pseudopotential was selected to treat the calculation and the cutoff energy was set as 820 eV.[45] Convergence tolerance parameters were set strictly as energy 1×10^{-5} eV per atom, force 3×10^{-2} eV $Å^{-1}$, stress 5×10^{-2} GPa, and displacement 1×10^{-3} Å. Monkhorst–Pack grid parameters were set as $4 \times 4 \times 4$ during the geometry optimization task.[46] The lattice constant was adjusted directly to modulate the corresponding strain conditions. The calculated bandgap values of $FAPbBr_3/CsPbBr_3$ materials kept a high consistency with previous studies, [47–49] which confirmed the validity of this calculation methodology.

Supporting Information

Supporting Information is available from the Wiley Online Library or from the author.

Acknowledgements

This work was supported by the National Natural Science Foundation of China (62174079) and the Science, Technology and Innovation Commission of Shenzhen Municipality (Projects Nos. JCYJ20220530113015035, JCYJ20210324120204011, and KQTD2015071710313656).

Conflict of Interest

The authors declare no conflict of interest.

Data Availability Statement

The data that support the findings of this study are available from the corresponding author upon reasonable request.

Keywords

biexciton Auger recombination, core–shell perovskite nanocrystals, electronic structure, laser spectroscopy, shell thickness

Received: July 25, 2023
Revised: September 17, 2023
Published online: October 18, 2023

[1] I. Levchuk, A. Osvet, X. Tang, M. Brandl, J. D. Perea, F. Hoegl, G. J. Matt, R. Hock, M. Batentschuk, C. J. Brabec, *Nano Lett.* **2017**, *17*, 2765.
[2] A. Dutta, R. K. Behera, P. Pal, S. Baitalik, N. Pradhan, *Angew. Chem., Int. Ed.* **2019**, *58*, 5552.
[3] J.-N. Yang, T. Chen, J. Ge, J.-J. Wang, Y.-C. Yin, Y.-F. Lan, X.-C. Ru, Z.-Y. Ma, Q. Zhang, H.-B. Yao, *J. Am. Chem. Soc.* **2021**, *143*, 19928.
[4] J. Li, L. Xu, T. Wang, J. Song, J. Chen, J. Xue, Y. Dong, B. Cai, Q. Shan, B. Han, H. Zeng, *Adv. Mater.* **2017**, *29*, 1603885.
[5] Y. Rong, Y. Hu, A. Mei, H. Tan, M. I. Saidaminov, S. I. Seok, M. D. Mcgehee, E. H. Sargent, H. Han, *Science* **2018**, *361*, eaat8235.
[6] W. Tian, H. Zhou, L. Li, *Small* **2017**, *13*, 1702107.
[7] S. A. Veldhuis, P. P. Boix, N. Yantara, M. Li, T. C. Sum, N. Mathews, S. G. Mhaisalkar, *Adv. Mater.* **2016**, *28*, 6804.
[8] H. Lian, Y. Li, S. Saravanakumar, H. Jiang, Z. Li, J. Wang, L. Xu, W. Zhao, G. Han, *Coord. Chem. Rev.* **2022**, *452*, 214313.
[9] N. Wang, W. Liu, Q. Zhang, *Small Methods* **2018**, *2*, 1700380.
[10] R. Begum, M. R. Parida, A. L. Abdelhady, B. Murali, N. M. Alyami, G. H. Ahmed, M. N. Hedhili, O. M. Bakr, O. F. Mohammed, *J. Am. Chem. Soc.* **2017**, *139*, 731.
[11] G. H. Ahmed, J. K. El-Demellawi, J. Yin, J. Pan, D. B. Velusamy, M. N. Hedhili, E. Alarousu, O. M. Bakr, H. N. Alshareef, O. F. Mohammed, *ACS Energy Lett.* **2018**, *3*, 2301.
[12] A. Pan, B. He, X. Fan, Z. Liu, J. J. Urban, A. P. Alivisatos, L. He, Y. Liu, *ACS Nano* **2016**, *10*, 7943.
[13] G. H. Ahmed, J. Yin, R. Bose, L. Sinatra, E. Alarousu, E. Yengel, N. M. Alyami, M. I. Saidaminov, Y. Zhang, M. N. Hedhili, O. M. Bakr, J.-L. Brédas, O. F. Mohammed, *Chem. Mater.* **2017**, *29*, 4393.
[14] P. Reiss, M. Protière, L. Li, *Small* **2009**, *5*, 154.
[15] C. Zhang, J. Chen, L. Kong, L. Wang, S. Wang, W. Chen, R. Mao, L. Turyanska, G. Jia, X. Yang, *Adv. Funct. Mater.* **2021**, *31*, 2100438.
[16] G. H. Ahmed, J. Yin, O. M. Bakr, O. F. Mohammed, *ACS Energy Lett.* **2021**, *6*, 1340.
[17] M. R. Kar, S. Ray, B. K. Patra, S. Bhaumik, *Mater. Today Chem.* **2021**, *20*, 100424.
[18] S. Bhaumik, S. A. Veldhuis, Y. F. Ng, M. Li, S. K. Muduli, T. C. Sum, B. Damodaran, S. Mhaisalkar, N. Mathews, *Chem. Commun.* **2016**, *52*, 7118.
[19] W. Chen, S. Bhaumik, S. A. Veldhuis, G. Xing, Q. Xu, M. Grätzel, S. Mhaisalkar, N. Mathews, T. C. Sum, *Nat. Commun.* **2017**, *8*, 15198.
[20] C. Jia, H. Li, X. Meng, H. Li, *Chem. Commun.* **2018**, *54*, 6300.
[21] G. Kaur, K. Justice Babu, N. Ghorai, T. Goswami, S. Maiti, H. N. Ghosh, *J. Phys. Chem. Lett.* **2019**, *10*, 5302.
[22] C. Zhang, S. Wang, X. Li, M. Yuan, L. Turyanska, X. Yang, *Adv. Funct. Mater.* **2020**, *30*, 1910582.
[23] D. Kong, Y. Jia, Y. Ren, Z. Xie, K. Wu, T. Lian, *J. Phys. Chem. C* **2018**, *122*, 14091.
[24] J. P. Philbin, E. Rabani, *J. Phys. Chem. Lett.* **2020**, *11*, 5132.
[25] Z. Dang, J. Shamsi, F. Palazon, M. Imran, Q. A. Akkerman, S. Park, G. Bertoni, M. Prato, R. Brescia, L. Manna, *ACS Nano* **2017**, *11*, 2124.
[26] J. H. Noh, S. H. Im, J. H. Heo, T. N. Mandal, S. I. Seok, *Nano Lett.* **2013**, *13*, 1764.
[27] R. J. Sutton, G. E. Eperon, L. Miranda, E. S. Parrott, B. A. Kamino, J. B. Patel, M. T. Hörantner, M. B. Johnston, A. A. Haghighirad, D. T. Moore, H. J. Snaith, *Adv. Energy Mater.* **2016**, *6*, 1502458.
[28] Z. Liang, S. Zhao, Z. Xu, B. Qiao, P. Song, D. Gao, X. Xu, *ACS Appl. Mater. Interfaces* **2016**, *8*, 28824.
[29] X. Zhang, Z. Guo, R. Li, J. Yu, B. Yuan, B. Chen, T. He, R. Chen, *ACS Appl. Mater. Interfaces* **2021**, *13*, 58170.
[30] V. I. Klimov, *Ann. Rev. Condens. Matter Phys.* **2014**, *5*, 285.
[31] J. A. Castañeda, G. Nagamine, E. Yassitepe, L. G. Bonato, O. Voznyy, S. Hoogland, A. F. Nogueira, E. H. Sargent, C. H. B. Cruz, L. A. Padilha, *ACS Nano* **2016**, *10*, 8603.
[32] L. Liu, H. Li, Z. Liu, Y.-H. Xie, *J. Colloid Interface Sci.* **2019**, *546*, 276.
[33] U. W. Pohl, in *Epitaxy of Semiconductors: Physics and Fabrication of Heterostructures*, Springer, Berlin **2020**.
[34] P. Scardi, A. Leonardi, L. Gelisio, M. R. Suchomel, B. T. Sneed, M. K. Sheehan, C.-K. Tsung, *Phys. Rev. B* **2015**, *91*, 155414.
[35] B. G. Chae, J. H. Lee, S. Park, E. Lee, C. M. Kwak, M. Jafari, Y. K. Jeong, C. G. Park, J. B. Seol, *ACS Nano* **2018**, *12*, 12109.
[36] W. M. Lai, D. Rubin, E. Krempl, in *Introduction to Continuum Mechanics*, Butterworth-Heinemann, Oxford **2009**.
[37] J. Cho, Y. K. Jung, J.-K. Lee, H.-S. Jung, *Langmuir* **2017**, *33*, 3711.
[38] Y. Gao, Y. Liu, F. Zhang, X. Bao, Z. Xu, X. Bai, M. Lu, Y. Wu, Z. Wu, Y. Zhang, Q. Wang, X. Gao, Y. Wang, Z. Shi, J. Hu, W. W. Yu, Y. Zhang, *Adv. Mater.* **2022**, *34*, 2207445.
[39] H. Hu, W. Guan, Y. Xu, X. Wang, L. Wu, M. Chen, Q. Zhong, Y. Xu, Y. Li, T.-K. Sham, X. Zhang, L. Wang, M. Cao, Q. Zhang, *ACS Nano* **2021**, *15*, 13129.
[40] C. Zhu, X. Niu, Y. Fu, N. Li, C. Hu, Y. Chen, X. He, G. Na, P. Liu, H. Zai, Y. Ge, Y. Lu, X. Ke, Y. Bai, S. Yang, P. Chen, Y. Li, M. Sui, L. Zhang, H. Zhou, Q. Chen, *Nat. Commun.* **2019**, *10*, 815.
[41] M. D. Segall, P. J. D. Lindan, M. J. Probert, C. J. Pickard, P. J. Hasnip, S. J. Clark, M. C. Payne, *J. Phys. Condes. Matter* **2002**, *14*, 2717.
[42] F. Pan, J. Li, X. Ma, Y. Nie, B. Liu, H. Ye, *RSC Adv.* **2022**, *12*, 1035.
[43] J. P. Perdew, K. Burke, M. Ernzerhof, *Phys. Rev. Lett.* **1996**, *77*, 3865.
[44] T. H. Fischer, J. Almlof, *J. Phys. Chem.* **1992**, *96*, 9768.
[45] D. R. Hamann, M. Schlüter, C. Chiang, *Phys. Rev. Lett.* **1979**, *43*, 1494.
[46] H. J. Monkhorst, J. D. Pack, *Phys. Rev. B* **1976**, *13*, 5188.
[47] G. Mannino, I. Deretzis, E. Smecca, A. La Magna, A. Alberti, D. Ceratti, D. Cahen, *J. Phys. Chem. Lett.* **2020**, *11*, 2490.
[48] J. Barichello, D. Di Girolamo, E. Nonni, B. Paci, A. Generosi, M. Kim, A. Levtchenko, S. Cacovich, A. Di Carlo, F. Matteocci, *Sol. RRL* **2023**, *7*, 2200739.
[49] L.-P. Cheng, J.-S. Huang, Y. Shen, G.-P. Li, X.-K. Liu, W. Li, Y.-H. Wang, Y.-Q. Li, Y. Jiang, F. Gao, C.-S. Lee, J.-X. Tang, *Adv. Opt. Mater.* **2019**, *7*, 1801534.